Yb^{3+} doped $Cs_2AgIn_{1-x}Bi_xCl_6$ Double Perovskite Nanocrystals

A Thesis

submitted in partial fulfilment of the requirements for the

BS-MS Dual Degree Programme

By

Shivam Yadav

(Reg. No. : 20151136)

Under the Supervision of

Dr. Angshuman Nag

Associate Professor, Department of Chemistry

Indian Institute of Science Education and Research(IISER)-Pune

Dr. Homi Bhabha Road, Pashan,

Pune (411008) INDIA.

March 2020

Declaration

I hereby declare that the matter embodied in the report entitled **"Yb^{3+} doped $Cs_2AgIn_{1-x}Bi_xCl_6$ Double Perovskite Nanocrystals"** are the results of the work carried out by me at the Department of Chemistry, IISER Pune, under the supervision of Dr. Angshuman Nag and the same has not been submitted elsewhere for any other degree.

Shivam Yadav

Date: 29th March 2020

Reg. No.: 20151136

Certificate

This is to certify that this dissertation entitled **"Yb^{3+} doped $Cs_2AgIn_{1-x}Bi_xCl_6$ Double Perovskite Nanocrystals"** towards the partial fulfilment of the BS-MS dual degree programme at the Indian Institute of Science Education and Research, Pune represents study/work carried out by **Shivam Yadav** at IISER Pune under the supervision of **Dr. Angshuman Nag**, Associate Professor, Department of Chemistry, IISER Pune during the academic year 2019-2020.

Supervisor

Dr. Angshuman Nag

Associate Professor

Department of Chemistry

IISER Pune

Date: 29th March 2020

Acknowledgements

- Supervisor: Dr. Angshuman Nag
  I want to thank him to allow me to work with him and to critically correct me every time. I'm learning from him to be discipline, to increase scientific temperament and be critical.
- TAC: Dr. Partha Hazra
  For evaluating my mid-year work.
- Vikash Kumar Ravi
  He is a friend cum mentor to me and has a major role in completion of this project. I want to thank him for being there always.
- Habibul Arfin
  For reviewing my work and help me to improve it throughout this project.
- All other lab members
  Every lab membered helped me in some way or the other, more importantly thank everyone for keeping the lab atmosphere lively.

Table of Contents

List of Figures

List of Table

Abstract

$Cs_2AgInCl_6$ is a direct band gap double perovskite (DP) having thermal and moisture stability. However, $Cs_2AgInCl_6$ exhibits wide band gap with poor optical absorption and emission in the visible region. Incorporation of Bi in the form of $Cs_2AgIn_{1-x}Bi_xCl_6$ alloy introduce a new lower energy absorption channels because of the Bi^{3+} $6s^2$ electrons. Also Bi^{3+} incorporation increases the intensity of broad visible-light emission. In this thesis, we have prepared colloidal Yb^{3+} doped $Cs_2AgIn_{1-x}Bi_xCl_6$ nanocrystals (NCs). The Yb^{3+} dopants introduce near-infrared (NIR) emission with peak at ~996 nm corresponding to $^2F_{5/2} \rightarrow {}^2F_{7/2}$ transition of Yb^{3+} f-electrons. Whereas, the NCs provides solution processability, which is required for fabrication of any thin film device. We have optimized the Yb^{3+} and Bi^{3+} concentration to get the high NIR emission at low excitation energy. Alloying with Bi^{3+} decreases the excitation energy such that commercial UV light emitting diodes (LEDs) can be used for excitation source. Future work in this direction may lead to the development NIR LEDs.

1 Introduction

1.1 Introduction to Metal Halide Perovskites and Double Perovskites:

Perovskites are materials having a crystal structure with the general formula ABX_3, where 'A' (bigger cation) occupies the corners, 'B' (cation) occupies bodycenter position, and 'X' (anion) occupies the facecenter position of the unit cell (Fig. 1).

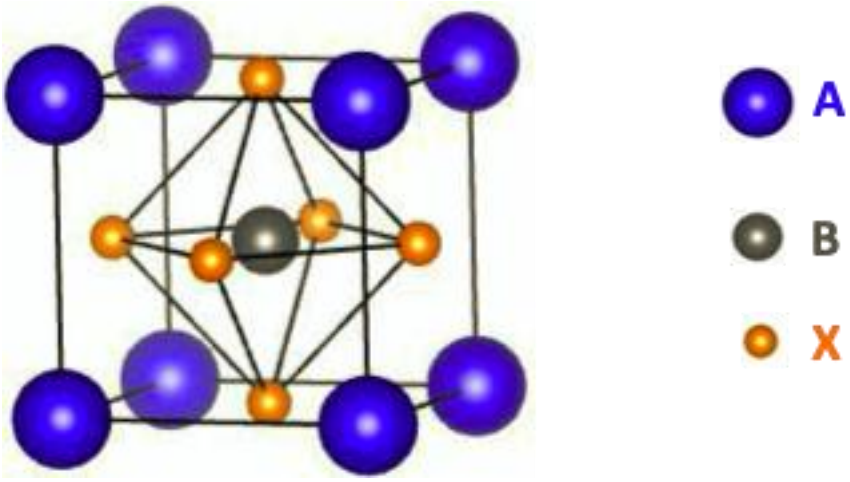

Fig. 1: Schematics showing perovskite crystal structure with ABX_3 generic composition.

In this category, lead halide perovskites (LHPs) with general formula $APbX_3$ ($A = Cs^+$, CH^{3+}; $X = Cl^-$, Br^-, I^-) have been extensively studied in the last decade.[1-8] LHPs show excellent optical and optoelectronic properties due to their high optical absorption cross-section, high luminescence efficiency and defect tolerant nature. Hence LHPs are promising materials for solar cells, lasers, light emitting diodes (LEDs), and photodetectors. Despite these outstanding properties, LHPs have some challenges such as lead toxicity and its moisture and thermal instability.

Extensive research has been done to explore different possibilities of Pb-free, thermal and moisture stable metal halide perovskite without significantly compromising intrinsic properties of LHPs.[9-13] One such strategy is to replace Pb^{2+} by another less toxic isovalent cation of the same group IV, like Sn^{2+} or Ge^{2+}. However, they do not form stable samples because of the rapid oxidation of Sn^{2+} or Ge^{2+} to the Sn^{4+} or Ge^{4+} respectively.[12, 14] Another popular replacement of Pb^{2+} is by heterovalent B^{3+} (B^{3+} = Bi^{3+}, Sn^{3+}), where three Pb^{2+} from $A_3Pb_3X_9$ ($3[APbX_3]$) are replaced with two B^{3+}, which leads to $A_3B_2X_9$.[15-18] Similarly, $A_2B(IV)X_6$ synthesis is tried to replace two Pb^{2+} with B^{4+} where B = Pd, Sn etc.[19, 20] See Fig. 2 for schematic representations for these different kinds of metal halide perovskite structure. The problem with these heterovalent replacements is that they lower the dimensionality of LHPs from 3D interconnected octahedra to 2D or even 0D to maintain the charge neutrality. This lowering in dimensionality restricts the mobility of charge carriers and thus affects optoelectronic properties. These drawbacks in different Pb-free perovskite further leads to the search of more feasible metal halide perovskites.

So to form stable 3D Pb-free metal halide perovskite having charge neutrality, 2 Pb^{2+} from LHPs are replaced with one monovalent (B^+) and one trivalent (B^{3+}) metal cation.[21-23] This forms the popularly known double perovskites (DPs) crystal structure with general formula $A_2B(I)B(III)X_6$; where B(I) = Ag^+, Cu^+, Na^+; and B(III) = In^{3+}, Bi^{3+}, Sb^{3+}. In general, DPs show good stability against light, heat, moisture. However, they possess either wide or indirect band gaps. Also in some cases, the optical transitions across the band gap are parity forbidden optical transition.[24] Therefore, to increase the optical activity of DPs in the visible and near infrared (NIR) region, doping or alloying with different metal ions has been explored.[25, 26] Also, alloying or doping of metal ions in DPs has been tried to tune the bandgap from indirect to direct, and/or changing the parity from forbidden to allowed by reducing the crystal symmetry of the

system.[27] One such example is reported by Luo et al.[28] which shows record PLQY ≈ 86% for Bi^{3+} doped $Cs_2Ag_{0.6}Na_{0.4}InCl_6$ powder.

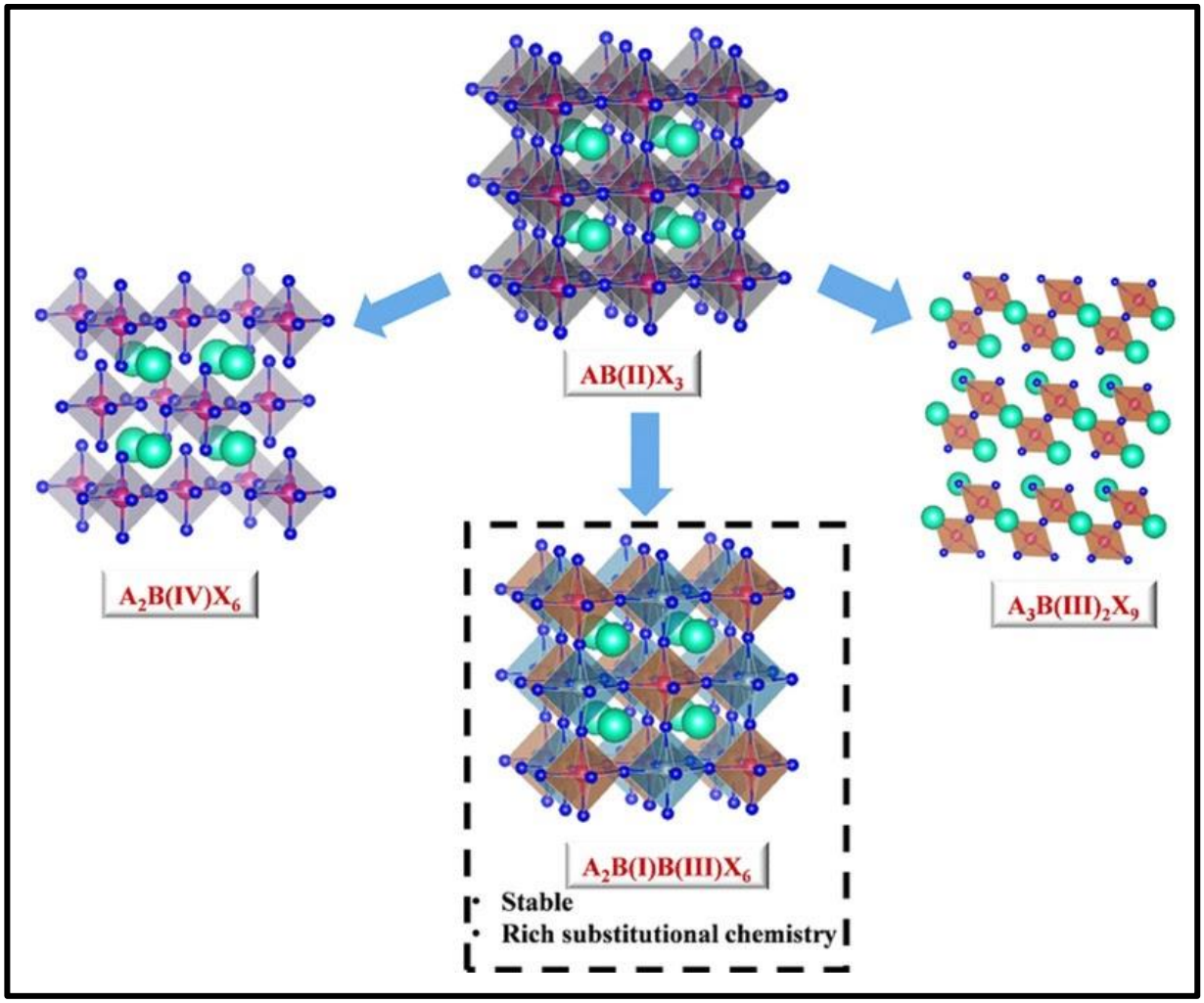

Fig. 2: Schematic representation of different metal halide perovskite structures. A-site cations are represented in green, B^{I}, B^{II}, B^{III} and B^{IV} cations are represented in pink and halide (X) anions are represented in blue colour. Reprinted with permission from ref.[29] Copyright 2020 WILEY-VCH Verlag GmbH.

1.2 Lanthanide (Ln^{3+}) Doping into Metal Halide Perovskites:

Lanthanides (Ln^{3+}) exhibit sharp f-f inner core electronic transitions, resulting into intense, sharp and stable luminescence.[30] But Ln^{3+} ions need sensitized by a host, where the host absorbs the light energy, and then non-radiatively transfers the energy to the Ln^{3+} ions. Then the Ln^{3+} de-excite by emitting light. Fig. 3 depicts f-electronic states of different lanthanides. Our choice of lanthanide ion is Yb^{3+} because it has the least complicated energy levels (Fig. 3) emitting in the near infrared (~996 nm) region

due to transition from $^2F_{5/2} \rightarrow {}^2F_{7/2}$ transitions. This Yb^{3+} is useful for luminescent solar concentrator, quantum cutting layer on solar cell and remote sensing.

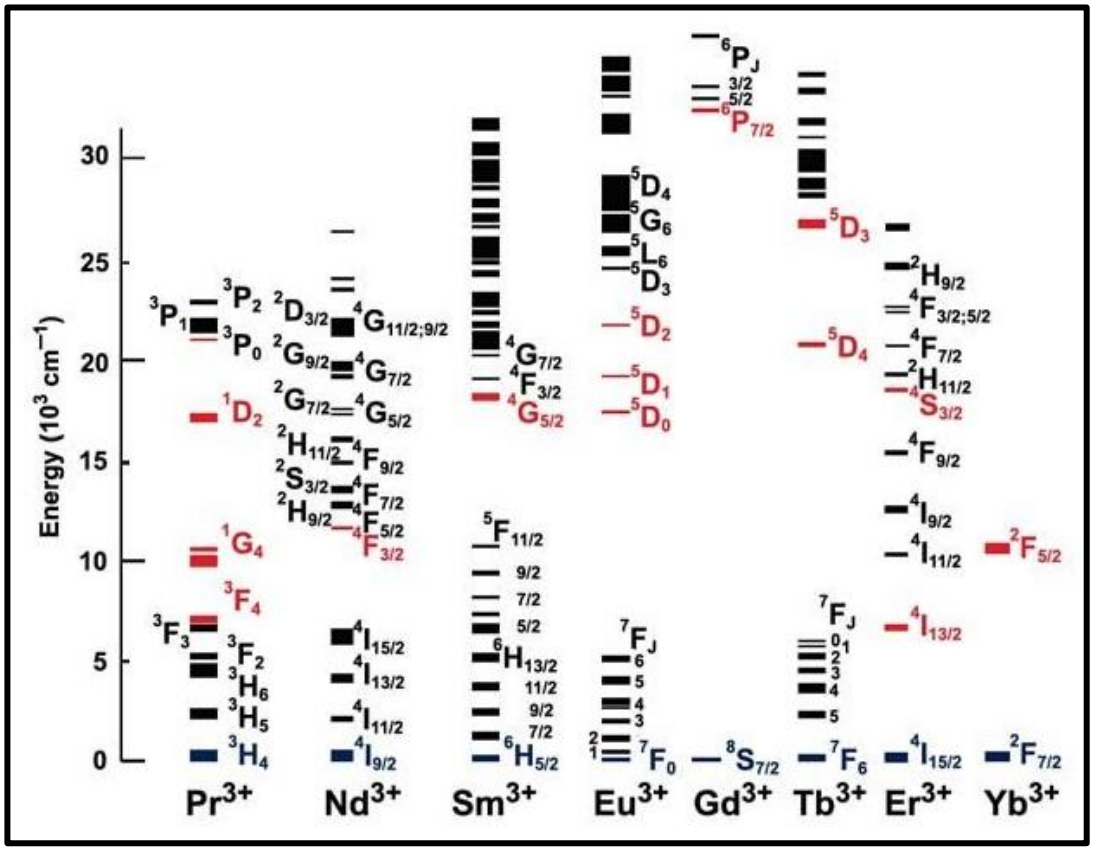

Fig. 3: Energy level diagram of different lanthanide (Ln^{3+}) ions where the ground state are represented by blue and the main energy level by red colour. Reprinted with permission from ref[31].

1.3 Scope of the Present Thesis:

Ln^{3+} ions like Yb^{3+} require an appropriate host material. Prior attempts of doping Ln^{3+} in semiconductor hosts were largely unsuccessful, become traditional semiconductors like Si, CdSe, GaAs, and $CuInSe_2$ offers tetrahedral sites to incorporate Ln^{3+} ions. But Ln^{3+} ions are big in size, and therefore require coordination number (CN) ≥ 6.[32] In this regards, metal halide perovskites semiconductors like $CsPbX_3$ are successfully doped by Yb^{3+}.[33-35] Yb^{3+} doping in Pb-free DP like $Cs_2AgInCl_6$ has also been attempted.[36] Recently, Arfin et al. reported Bi^{3+}-Ln^{3+} (Ln = Yb and Er) codoped $Cs_2AgInCl_6$ microcrystals, with strong near infrared emission at 994 nm and 1540 nm, for the Yb and Er f-f transitions.[26] Codoping Bi^{3+} into the $Cs_2AgInCl_6$ lattice introduces new states near the band edges owing to the Bi $6s^2$ electrons, and thereby introduces lower

energy absorption channels (~370 nm).[26, 37] This decrease in optical excitation energy helps to excite the samples using commercially available UV LEDs.

But the microcrystals of Bi^{3+}-Yb^{3+} codoped $Cs_2AgInCl_6$ cannot be processed in the film form, which is required for any optoelectronic device. To address this issue, we planned to design solution processed nanocrystals (NCs) of Yb^{3+} doped $Cs_2AgIn_{1-x}Bi_xCl_6$, and study their optical absorption and emission properties. Fig. 4 shows the schematic structure of Yb^{3+} doped $Cs_2AgIn_{1-x}Bi_xCl_6$ DP.

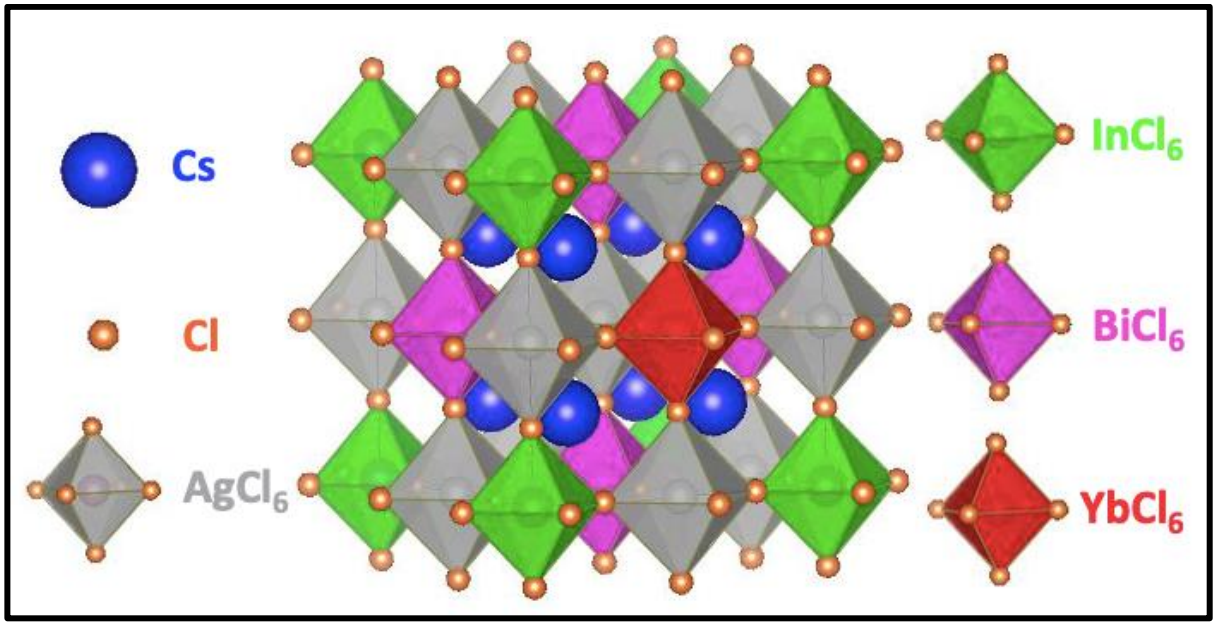

Fig. 4: Schematic crystal structure of Yb^{3+} doped $Cs_2AgIn_{1-x}Bi_xCl_6$ double perovskite.

2 Experimental Sections

2.1 Chemicals:

Cesium carbonate (Cs_2CO_3, 99.9%), bismuth (III) chloride ($BiCl_3$, 99.99%), silver nitrate ($AgNO_3$, 99.99%), indium(III) chloride ($InCl_3$, anhydrous powder, ≥99.999%), ytterbium (III) chloride hexahydrate ($YbCl_3.6H_2O$, 99.9%), oleylamine (OLA, 70%),1-octadecene (ODE) and oleic acid (OA, 90%) were purchased from Sigma-Aldrich. Ethyl acetate, Hydrochloric acid (HCl, 35 wt. %) and n-hexane were purchased from Rankem, India. Chemical are used as it is after purchasing without further purification.

2.2 Cesium Oleate Preparation:

Cs-oleate is prepared following a prior report.[38] 0.814gm Cesium carbonate in 2.5 mL OA and 10 mL ODE are taken in three-neck 50 mL round-bottom (RB) flask. The mixture is then put in vacuum at 120 °C for 1 hour. Then temperature is raised to 150

°C till the solution get clear. This Cs-oleate formed is then kept under nitrogen atmosphere for further use. The Cs-oleate stock solution is the source of Cs precursor and it is preheating at 110 °C for 10-15 min before injecting to reaction mixture for NC synthesis.

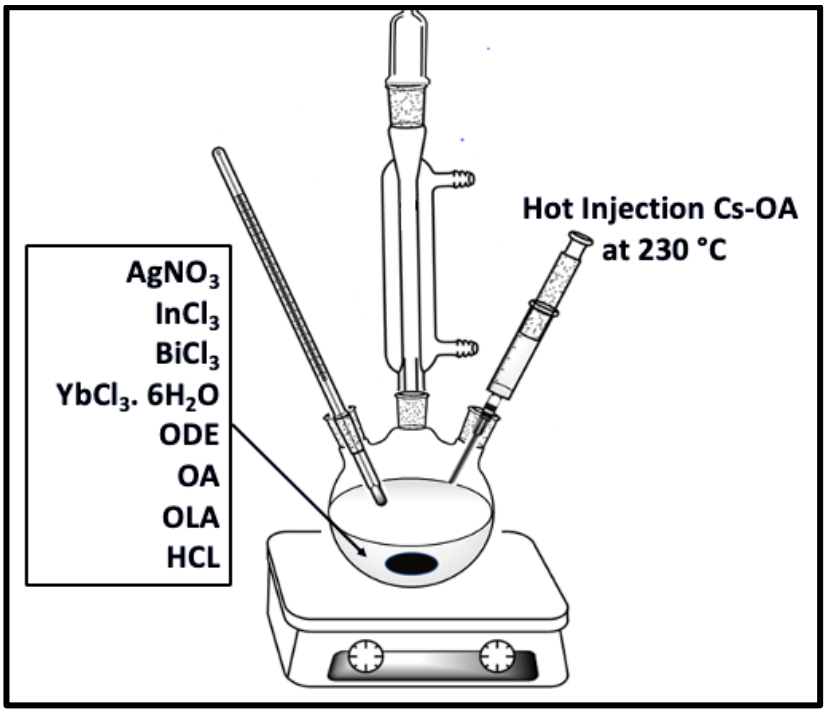

Fig. 5: Synthesis illustration of Yb^{3+} doped $Cs_2AgIn_{1-x}Bi_xCl_6$ double perovskite nanocrystals.

2.3 Synthesis of Yb^{3+} doped $Cs_2AgIn_{1-x}Bi_xCl_6$ Nanocrystals:

Synthesis of Yb^{3+} (50% of In precursor) doped $Cs_2AgIn_xBi_{1-x}Cl_6$ (x = 0, 0.03, 0.05, 0.1, 0.15, 0.20, 1) NCs is carried out by following the report of Liu et al with some modification.[38] In a typical synthesis $AgNO_3$ (0.36 mmol), $InCl_3$ (0.36 mmol), $YbCl_3.6H_2O$ (0.18 mmol), with varied amount of $BiCl_3$ (from 0% to 100% of $InCl_3$) along with 1 mL OA, 14 mL ODE, 1 mL OLA and 0.28 mL HCl are taken in a three-neck flask. This reaction mixture is heated till 120 °C under N_2 atmosphere and then degassed for 1 hour. The temperature is then raised till 230 °C under inert atmosphere, and at this temperature, 0.8 mL preheated (at 110 °C) stock solution of Cs-oleate is injected quickly under vigorous stirring. Then the reaction is quenched by adding ~10 mL ODE within 5 second and then immersing the RB in an ice bath. The reaction product is purified first by centrifuging the crude mixture at 7800 rpm for 7 min throwing

the supernatant and then repeating the same process twice by re-dispersion the precipitate in 3 mL hexane.

The precipitate obtained after third washing is again dispersed in 3 mL hexane and then centrifuge at 4000 rpm for 5 minute. The obtained supernatant is our final product containing colloidal NCs, and is stored for further studies. After optimizing Bi concentration, $YbCl_3.6H_2O$ precursor content is varied to achieve the most intense NIR emission.

2.4 Characterization Techniques:

Powder x-ray diffraction (PXRD) data were recorded using a Bruker D8 Advance X-ray diffraction machine equipped with Cu Kα (1.54 Å) radiation by drop casting NCs over a glass slide. UV-visible absorption spectra of colloidal NCs are measured using a Cary series UV visible spectrophotometer. Steady-state photoluminescence (PL), PL excitation (PLE) spectra are recorded using Edinburgh FLS 980 (Edinburgh Instruments) spectrophotometer. Transmission electron microscopy (TEM) images and high-resolution TEM (HRTEM) images are captured by using a UHR FEG-TEM, JEOL JEM 2200Fs field emission transmission electron microscope at 200 kV. TEM samples are prepared by drop-casting a dilute dispersion of samples on a carbon-coated Cu TEM grid. Field emission scanning electron microscopy (FESEM) imaging and elemental analysis by energy-dispersive X-ray spectroscopy (EDS) are carried out by using a Zeiss Ultra Plus field emission FESEM instrument.

3 Results and Discussion

3.1. Optimizing Bi^{3+} in $Cs_2AgIn_{1-x}Bi_xCl_6$ NCs having fixed Yb^{3+} concentration

3.1.1. Composition, structure and morphology of Yb^{3+} doped $Cs_2AgIn_{1-x}Bi_xCl_6$ NCs:

Bi^{3+} precursor is varied from 0% to 100% with respect to In^{3+} precursor, keeping the concentration of Yb^{3+} precursor fixed at 50% of In precursor. Elemental analysis of the product Yb^{3+} doped $Cs_2AgIn_{1-x}Bi_xCl_6$ NCs is done by EDS. The elemental compositions of product NCs are summarized in Table 1. Clearly, with increase in Bi^{3+} precursor concentration, Bi^{3+} contribution in the product (“x”) increases systematically. Yb^{3+} doping % turn out to be constant at ~ 6% for different values of “x”.

Table 1: Comparison of elemental compositions precursor with that of Yb^{3+} doped $Cs_2AgIn_{1-x}Bi_xCl_6$ product NCs obtained by EDS.

Precursor↓	Yb^{3+} doped $Cs_2AgIn_{1-x}Bi_xCl_6$								
Yb^{3+}	0%	50%	50%	50%	50%	50%	50%	50%	0%
x	0	0	0.03	0.05	0.1	0.15	0.2	1	1
Elemental composition obtained by EDS data									
Yb^{3+}	0	7%	5%	8%	5%	6%	8%	8%	0%
x	0	0	0.05	0.07	0.11	0.14	0.17	1	1

The portion of precursor incorporating in final product is much higher for Bi^{3+} in comparison to Yb^{3+}. Bi^{3+} can completely replace In forming $Cs_2AgBiCl_6$ (x = 1) NCs. But Yb^{3+} incorporation remains to only a few percentage. Therefore, we term $Cs_2AgIn_{1-x}Bi_xCl_6$ alloy NCs with x varying throughout the range of 0 to 1, whereas, Yb^{3+} incorporation is in the form doping.

For these above Yb^{3+} doped $Cs_2AgIn_{1-x}Bi_xCl_6$ NCs samples, PXRD patterns along with their reference patterns for bulk $Cs_2AgInCl_6$ and $Cs_2AgBiCl_6$ are shown in Fig. 6 (a).

The PXRD patterns of Yb^{3+} doped $Cs_2AgIn_{1-x}Bi_xCl_6$ NCs agree well with the $Cs_2AgInCl_6$ and $Cs_2AgBiCl_6$ references thus all the compositions have the same elpasolite cubic crystal structure. $Cs_2AgInCl_6$ crystallizing in the $Fm\bar{3}m$ space group. Magnified PXRD pattern in Fig. 6(b) infers a systematic shift of (220) peak at $2\theta \sim 24°$ towards lower 2θ with increasing x. This peak shift is because of increase in inter planar distance (d) when smaller sized In^{3+} (0.92 Å) ions substituted by bigger Bi^{3+} (1.17 Å) ion, with increasing x. Since the Yb^{3+} doping is similar for all the samples with varying "x", the contribution of Yb^{3+} in the observed lattice expansion is negligible. This systematic shift at $2\theta \sim 24°$ peak suggest that both Bi^{3+} and In^{3+} ions are part of the lattice of $Cs_2AgIn_{1-x}Bi_xCl_6$ alloy NCs.

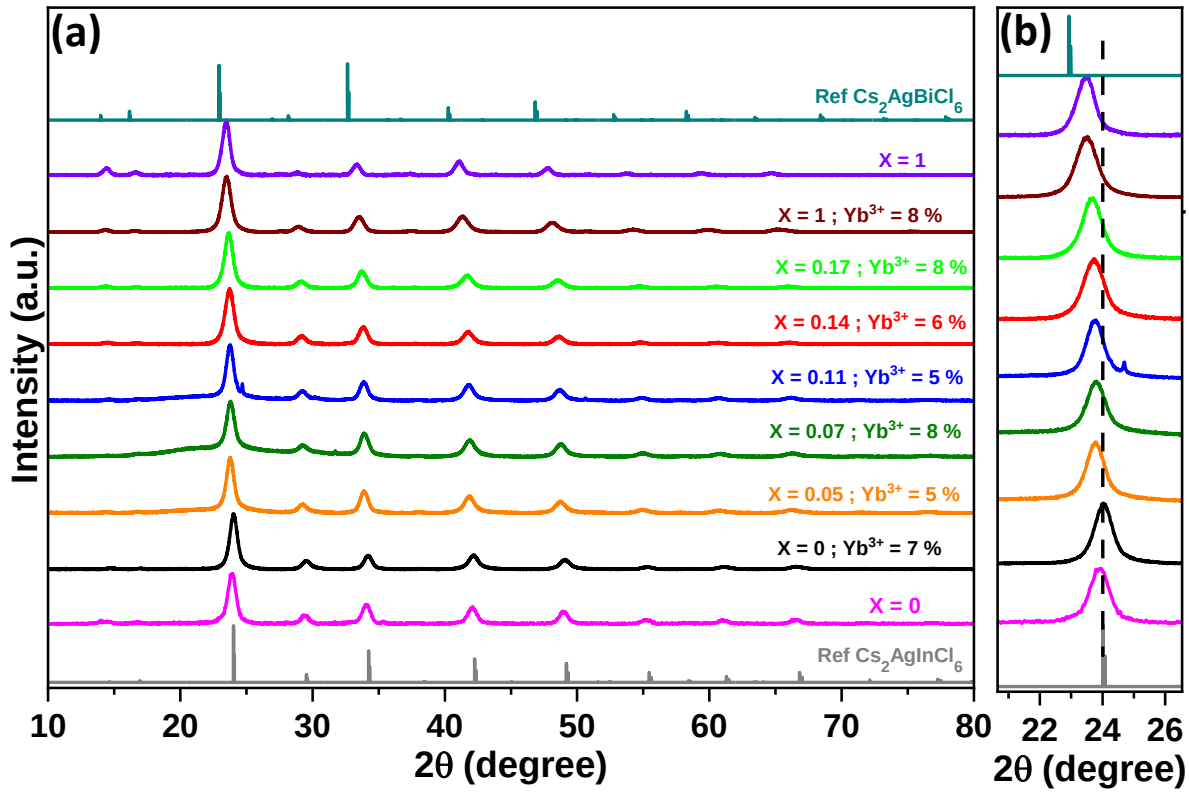

Fig. 6: (a) PXRD patterns of Yb^{3+} doped $Cs_2AgIn_{1-x}Bi_xCl_6$ double perovskite NCs. (b) Magnified view of the PXRD patterns of (a) showing shift in (220) plane peak at 2θ ~ 24°. The Yb^{3+} concentrations remain constant in the range of 5% to 8% of In^{3+} concentration for different samples.

TEM images in Fig. 7 (a) and (b) show the cuboid morphology of 7% Yb^{3+} doped $Cs_2AgIn_{0.95}Bi_{0.05}Cl_6$ NCs and 6% Yb^{3+} doped $Cs_2AgIn_{0.86}Bi_{0.14}Cl_6$ NCs respectively. The size distribution histogram shows that the average edge length of 7% Yb^{3+} doped $Cs_2AgIn_{0.95}Bi_{0.05}Cl_6$ NCs is 9.4 ± 1.4 nm (Fig. 7 (c)) and that of 6% Yb^{3+} doped $Cs_2AgIn_{0.86}Bi_{0.14}Cl_6$ NCs is 10.9 ± 2.0 nm (Fig. 7 (d)). These results suggest that on increasing the Bi^{3+} concentration, the size of the NCs increases slightly, although their shape seems to be cuboid in both cases. However, the observation needs to be verified with TEM measurements on more number of samples. HRTEM image in Fig. 7 (e) and (f) show high crystallinity of the NCs. The labelled lattice fringes in HRTEM images show inter planar distance of 3.8 Å (Fig. 7 e and f) corresponding to (220) plane with XRD peak at 2θ ~ 24° (Fig. 6). Similarly, 2.6 Å (Fig. 7e) and 2.7Å (Fig. 7f) are interplanar distances that match with (400) plane with XRD peak at 2θ ~ 34° of the $Cs_2AgInCl_6$.

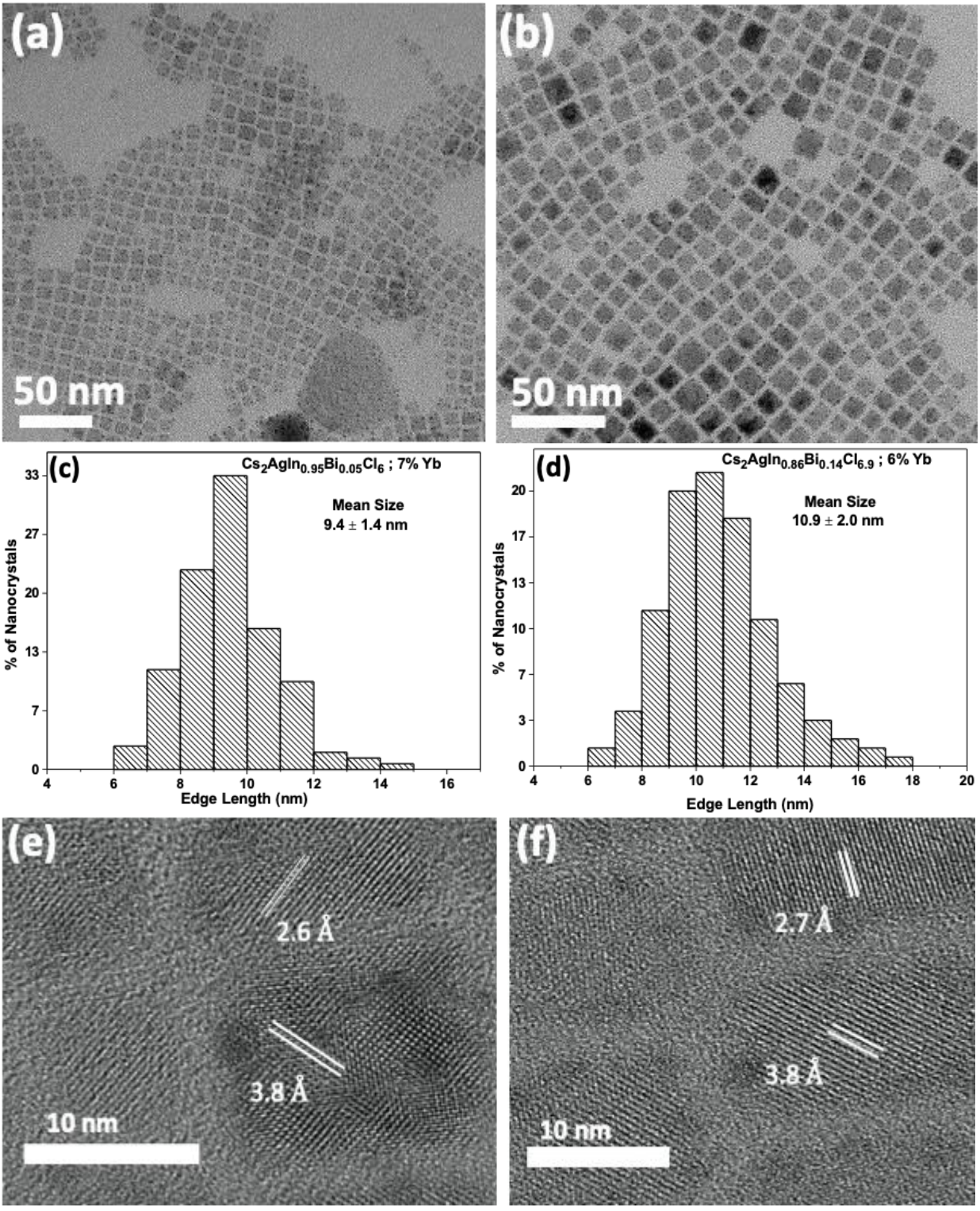

Fig. 7: (a-b) TEM images, (c-d) size distribution histogram and (e-f) HRTEM images of 7%Yb^{3+} doped $Cs_2AgIn_{0.95}Bi_{0.05}Cl_6$ NCs (a, c, e) and 6%Yb^{3+} doped $Cs_2AgIn_{0.86}Bi_{0.14}Cl_6$ NCs (b, d, f).

3.1.2 Optical properties of Yb^{3+} doped $Cs_2AgIn_{1-x}Bi_xCl_6$ NCs:

Fig. 8 shows the UV-visible absorption spectra of Yb^{3+} doped $Cs_2AgIn_{1-x}Bi_xCl_6$ DP NCs. Incorporation of Bi^{3+} gives rise to a new absorption peak at 365 nm. The absorbance at 365 nm increases systematically with an increase in Bi^{3+} concentration. Other than ~365 nm peak, the absorption spectra are similar for all samples with an onset and ~330 nm and peaked around 240 nm. When In^{3+} is completely replaced by Bi^{3+} in 8% Yb doped $Cs_2AgBiCl_6$ (brown) and $Cs_2AgBiCl_6$(violet), absorption spectra show a hump at ~280 nm, which seems to be intrinsic of $Cs_2AgBiCl_6$ NCs.

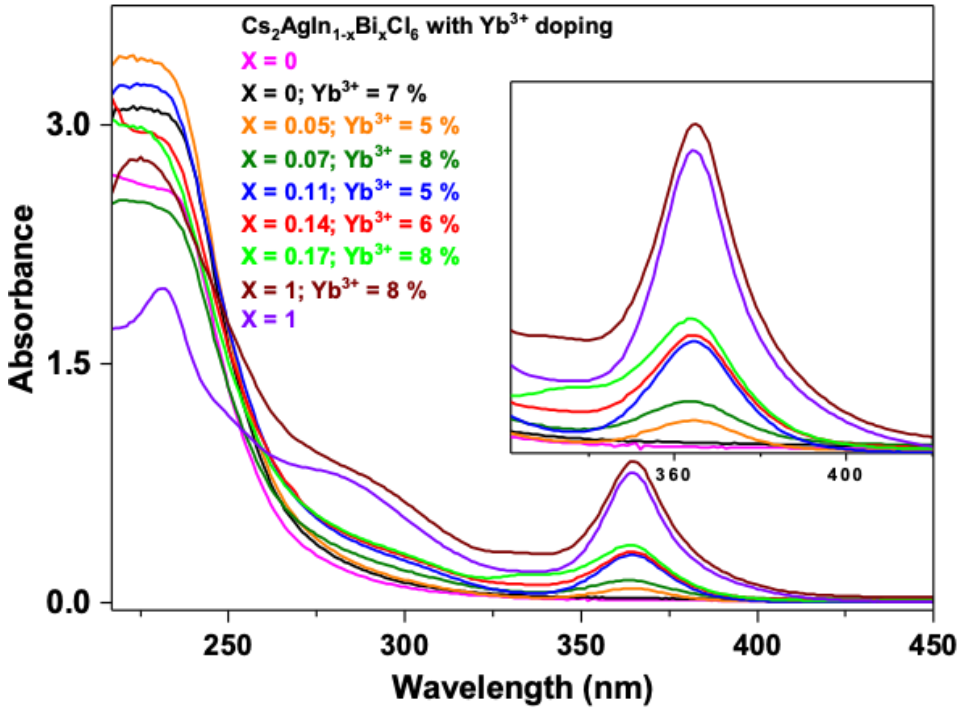

Fig. 8: UV-visible absorption spectra of colloidal Yb^{3+} doped $Cs_2AgIn_{1-x}Bi_xCl_6$ double perovskite NCs. Inset shows the magnified view of absorption spectra ~360 nm.

NIR PL spectra (Fig. 9a) of Yb^{3+} doped $Cs_2AgIn_{1-x}Bi_xCl_6$ DP NCs excited by 365 nm light exhibit down converted light emission with peak at 996 nm. This emission is due to $^2F_{5/2} \rightarrow {}^2F_{7/2}$ transitions of Yb^{3+} f electrons. Expectedly, PL spectra of undoped $Cs_2AgInCl_6$ (x = 0) and $Cs_2AgBiCl_6$ (x = 1) NCs do not show the NIR emission. It is to be noted that 7% Yb^{3+} doped $Cs_2AgInCl_6$ (black spectrum overlapped with spectra of undoped samples) also do not show the NIR emission. The NIR emission appears only for the Yb^{3+} host that contains Bi^{3+} (x > 0). This is because, in the absence of Bi^{3+} ions, the sample does not absorb the 365 nm light, as shown in Figure 8. The NIR emission intensity increases with increasing the Bi^{3+} concentration upto x = 0.14 and then

decreases with further increase Bi^{3+} concentration. Probably at very high Bi^{3+} concentration, the properties of the host tends to shift towards $Cs_2AgBiCl_6$ DP which is indirect band gap[39] semiconductor, unlike the direct band gap $Cs_2AgInCl_6$ DPs. Possibility of such direct to indirect transitions, and unknown defect state contributions might be the reasons for the decrease in NIR emission intensities at higher Bi^{3+} concentrations.

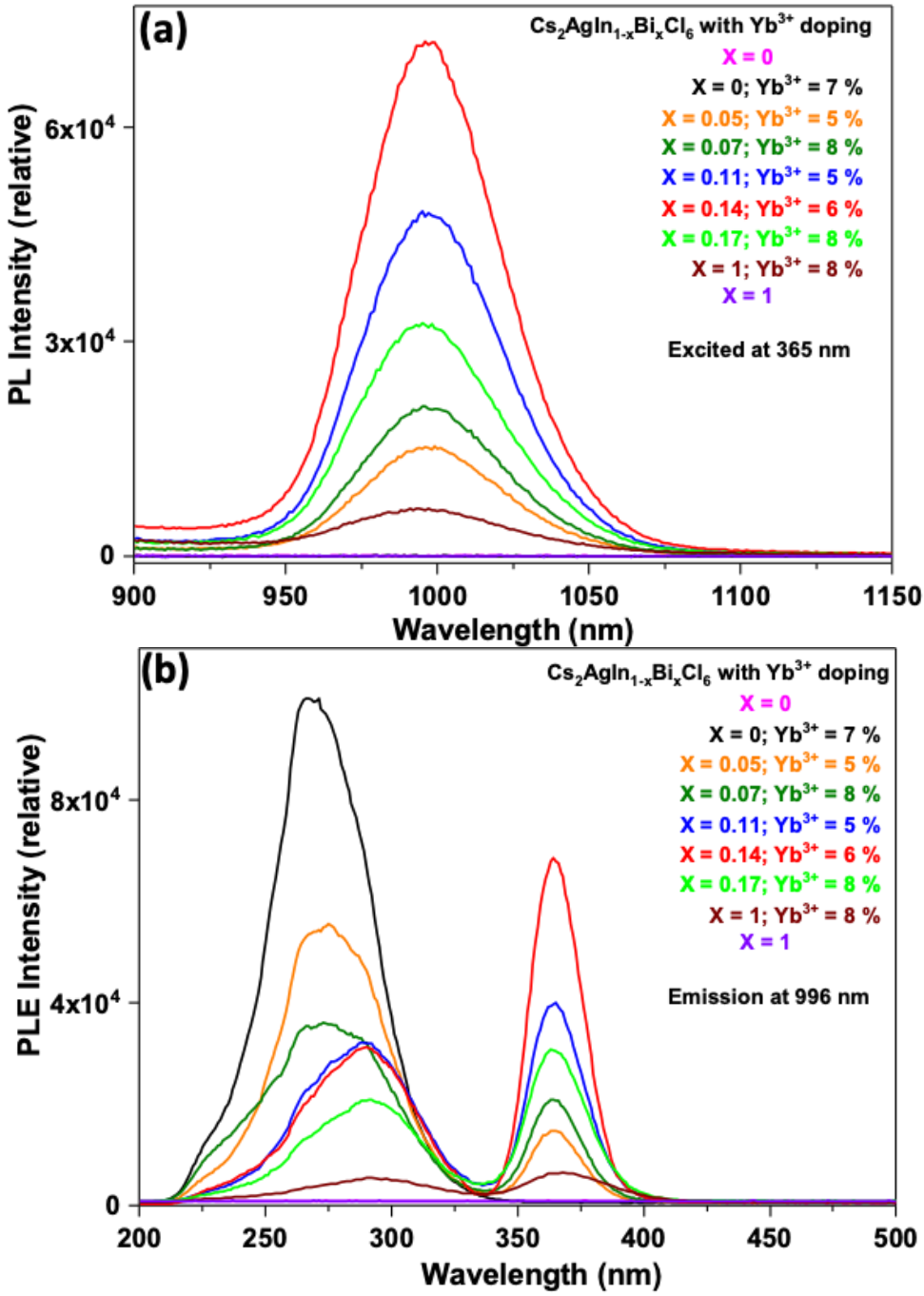

Fig. 9: NIR emission spectra (a) of Yb^{3+} doped $Cs_2AgIn_{1-x}Bi_xCl_6$ NCs excited by 365 nm. (b) PLE spectra of Yb^{3+} doped $Cs_2AgIn_{1-x}Bi_xCl_6$ NCs with emission fixed at 996 nm.

PLE spectra (Fig. 9b) obtained by measuring emission at 996 nm shows two peaks, one at ~365 nm which is due to Bi^{3+} related absorption, another centred at 265 nm corresponding to the $Cs_2AgInCl_6$ related absorption peak as shown in Figure 8. The NIR emission contribution by 265 nm excitation decreases continuously as Bi^{3+} concentration increases in Yb^{3+} doped $Cs_2AgIn_{1-x}Bi_xCl_6$ NCs. This decrease in PL intensity at 265 nm excitation is because of faster non-radiative relaxation excited carriers to lower lying states (corresponding to 365 nm excitation) introduced by Bi^{3+} incorporation in the host. As our focus is to decrease the optical excitation energy and increase NIR emission, so we finalize x = 0.14 as the optimized composition of host. This is because Fig. 9(a-b) shows 6% Yb^{3+} doped $Cs_2AgIn_{0.86}Bi_{0.14}Cl_6$ shows the most intense NIR emission at 365 nm excitation.

Other than Yb^{3+} NIR emission, $Cs_2AgIn_{1-x}Bi_xCl_6$ host itself emits in the visible region. Fig. 10 (a) shows broad PL spectra of Yb^{3+} doped $Cs_2AgIn_{1-x}Bi_xCl_6$ DP NCs in the visible region. Corresponding PLE spectra with emission fixed at 630 nm is shown in Fig. 10(b). The emission contribution by both 265 nm and 365 nm excitation is present for the hosts with x > 0. For samples x = 0, only 265 nm excitation leads to a weak emission at 630 nm. Increasing in Bi^{3+} concentration till x = 0.14 increases both the absolute intensity of visible light emission and the relative intensity of 365 nm PLE peak with respect to the 265 nm PLE peak. Similar broad visible light emission has been previously assigned to self-trapped excitons (STEs).[28] Fig. 9-10 shows that both the visible light and NIR light emissions are most intense for Yb^{3+} doped $Cs_2AgIn_{1-x}Bi_xCl_6$ NCs with x = 0.14.

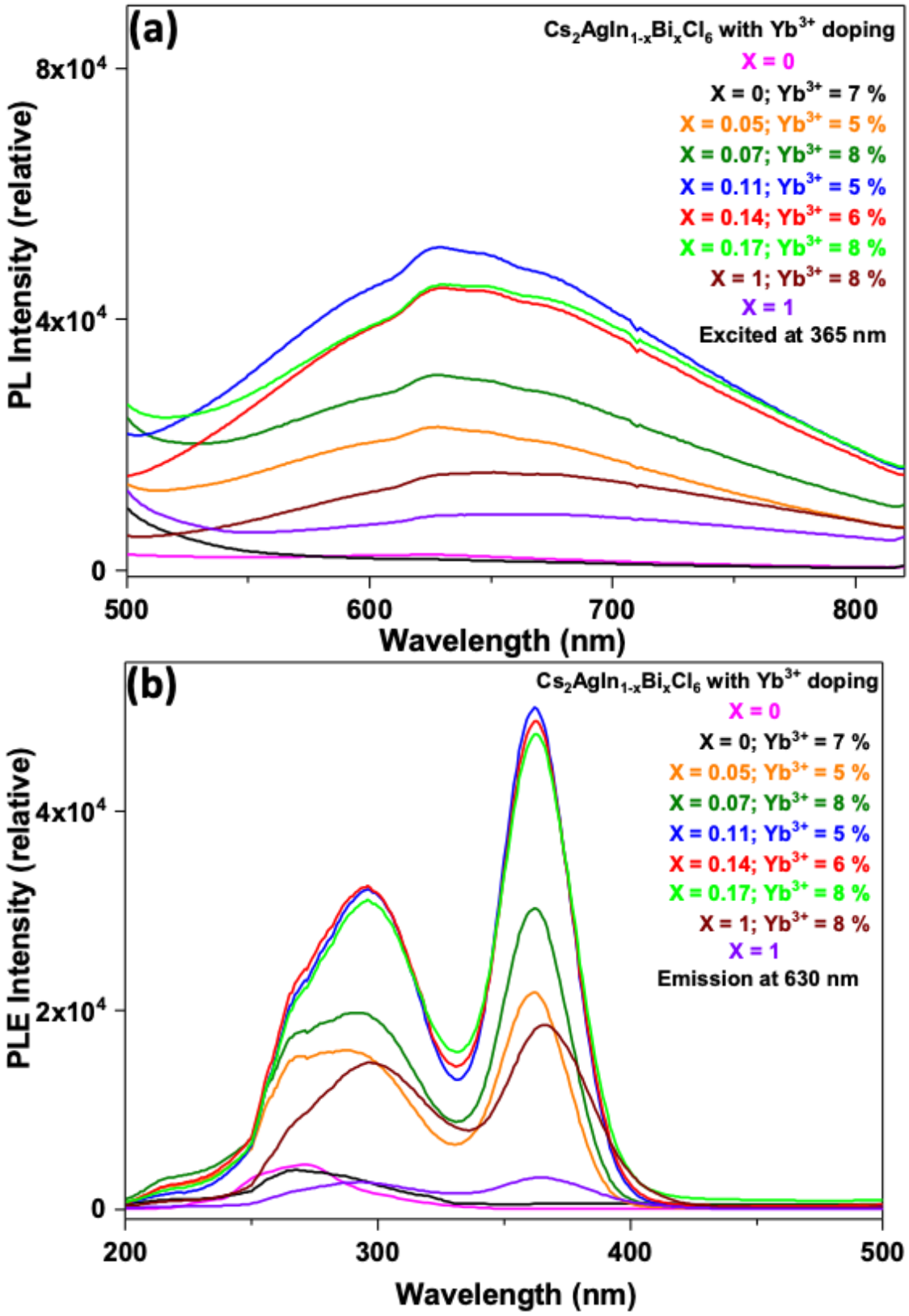

Fig. 10: (a) PL of Yb^{3+} doped $Cs_2AgIn_{1-x}Bi_xCl_6$ NCs in the visible region at 365 nm excitation. (b) PLE spectra of Yb^{3+} doped $Cs_2AgIn_{1-x}Bi_xCl_6$ NCs with emission fixed at 630 nm.

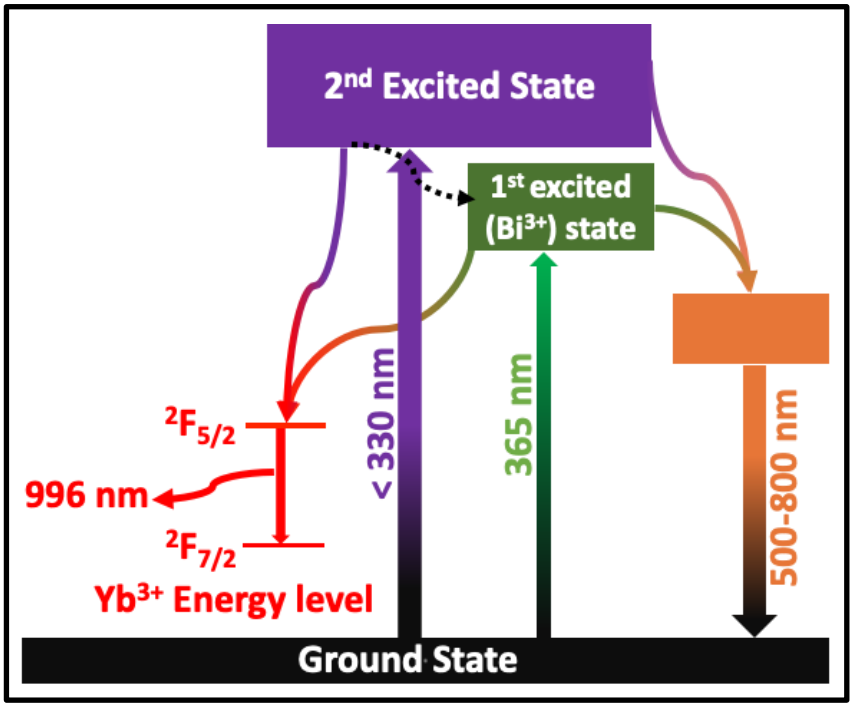

Fig. 11: Schematic energy level diagram of Yb^{3+} doped $Cs_2AgIn_{1-x}Bi_xCl_6$ DP.

The energy level diagram of Yb^{3+} doped $Cs_2AgIn_{1-x}Bi_xCl_6$ DP NCs shown in Fig. 11. For x = 0, the excitation happens at <330 nm. After Bi^{3+} alloying (x > 1) the excitation energy decreased to ~365 nm which is sufficient for excitation with ~365 nm UV LEDs. Both these excitations can give rise to both visible light emission of the host and NIR emission of Yb^{3+}. The excitation energy of the host is non-radiatively transferred to the Yb^{3+}, exciting their f-electrons. Subsequent de-excitation of f-electrons following $^2F_{5/2} \rightarrow {}^2F_{7/2}$ radiative transition gives rise to the NIR emission at 996 nm. The broad visible emission is probably via self-trapped excitons (STEs) following prior literature.[28]

3.2. Optimizing Yb^{3+} in $Cs_2AgIn_{1-x}Bi_xCl_6$ NCs having fixed Bi^{3+} concentration

3.2.1. Characterization of Yb^{3+} doped $Cs_2AgIn_{1-x}Bi_xCl_6$ NCs:

Yb^{3+} precursor is varied 25%, 50% and 100% with respect to In precursor, keeping the Bi^{3+} precursor concentration fixed at 15% of In precursor. The elemental composition of Yb^{3+} doped $Cs_2AgIn_{1-x}Bi_xCl_6$ NCs are summarized in Table. 2. Expectedly, Yb^{3+} concentration in the NCs increases with increasing Yb^{3+} precursor concentration. Bi^{3+} concentration in the NCs resembles with the amount of precursor used (15% of In precursor).

Table 2: Comparison of elemental compositions precursor with that of Yb^{3+} doped $Cs_2AgIn_{1-x}Bi_xCl_6$ product NCs obtained by EDS.

Precursor↓	Yb^{3+} doped $Cs_2AgIn_{1-x}Bi_xCl_6$		
Yb^{3+}	25%	50%	100%
x	0.15	0.15	0.15
Elemental composition obtained by EDS			
Yb^{3+}	4%	6%	15%
x	0.11	0.14	0.16

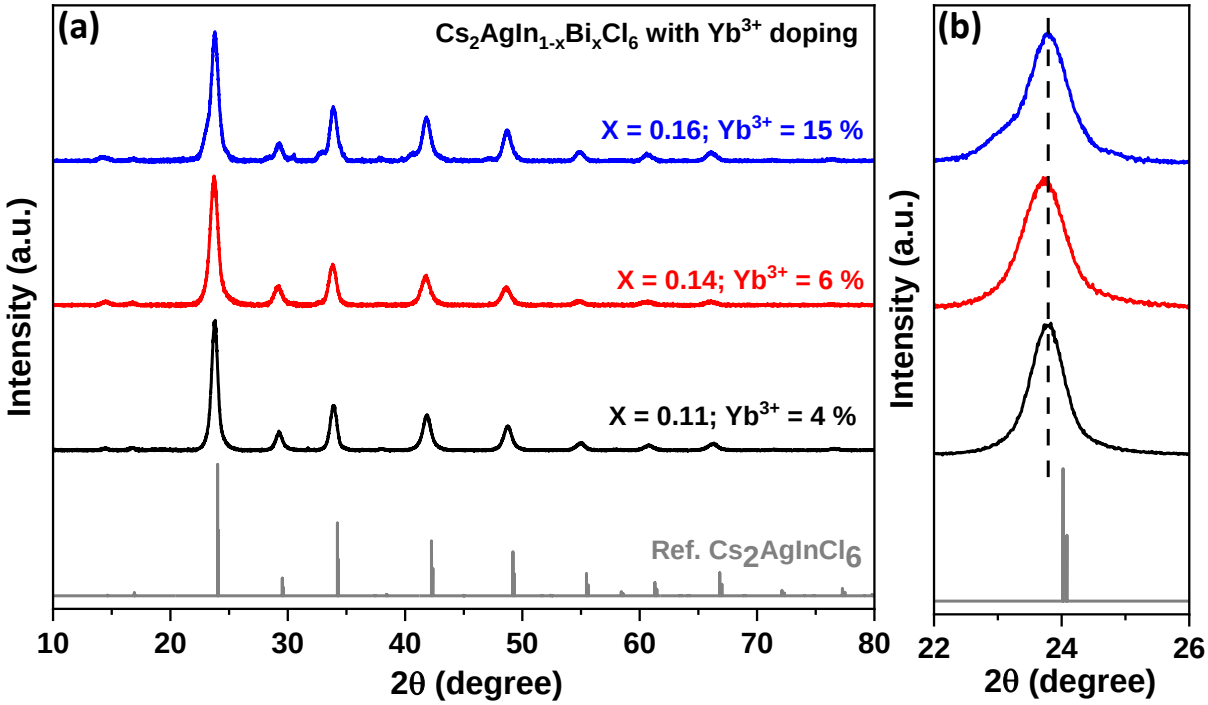

Fig. 12: (a) PXRD patterns of Yb^{3+} doped $Cs_2AgIn_{1-x}Bi_xCl_6$ double perovskite NCs. (b) Magnified view of the PXRD patterns of (a) showing shift in (220) plane peak at 2θ ~ 24°. The Bi^{3+} concentrations remain almost constant in range of 11% to 16% with respect to In^{3+} concentration in all three samples.

PXRD patterns of Yb^{3+} doped $Cs_2AgIn_{1-x}Bi_xCl_6$ NCs matches with the reference pattern of bulk $Cs_2AgInCl_6$ shown in Fig. 12a. Magnified view of the PXRD patterns around 2θ ~ 24° peak (Fig. 12 b) doesn't show any significant shift because ionic sizes of both In^{3+} (0.92 Å) and Yb^{3+} (0.98 Å) are similar in octahedral geometry. Also the difference in Bi^{3+} concentrations in all three samples is not significant enough to observe a visible shift in XRD peaks.

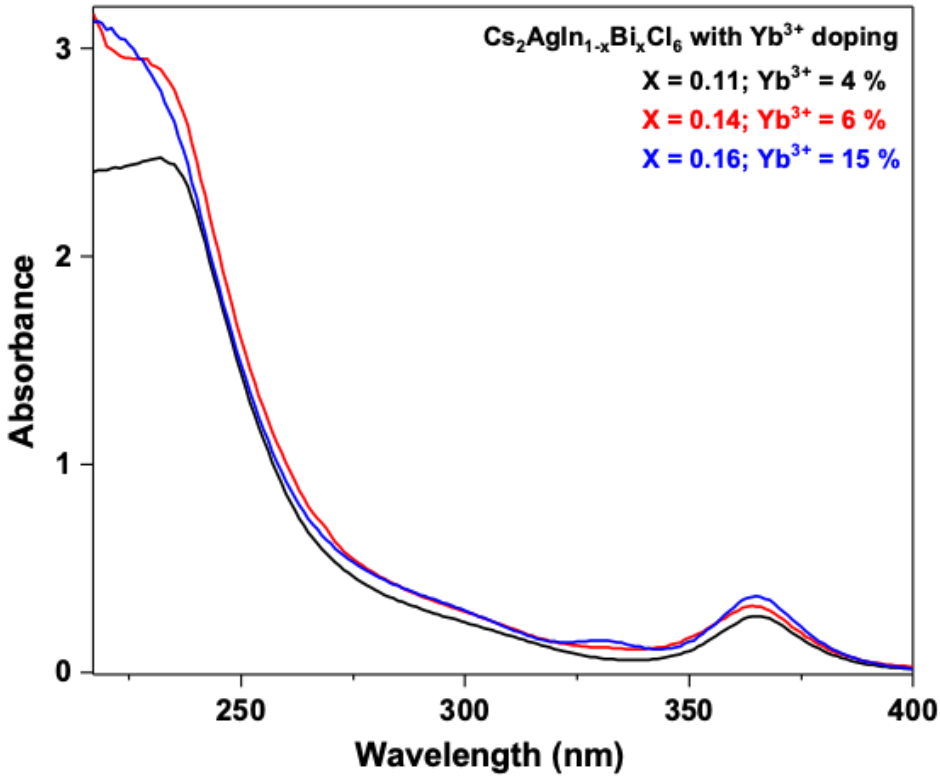

Fig. 13: Optical absorption spectra of colloidal Yb^{3+} doped $Cs_2AgIn_{1-x}Bi_xCl_6$ double perovskite NCs.

3.2.2 Optical properties of Yb^{3+} doped $Cs_2AgIn_{1-x}Bi_xCl_6$ NCs

The UV absorption spectra (Fig. 13) of all the Yb^{3+} doped $Cs_2AgIn_{1-x}Bi_xCl_6$ DP NCs are similar with a absorption peak ~365 nm peak due to Bi^{3+} energy level. The absorption spectra for all the three samples are similar with onset for second absorption at ~330 nm and a peak around at 240 nm. NIR PL spectra of Yb^{3+} doped $Cs_2AgIn_{1-x}Bi_xCl_6$ double perovskite NCs excited by 365 nm light are shown in Fig. 14 (a) and PLE spectra obtained by measuring emission at 996 nm in Fig.14 (b). The PL intensity is similar for 4% and 6% Yb^{3+} and then decreased slightly for 15% Yb^{3+} doping concentration (Fig. 14 b). However, the difference in NIR emission intensity between these three samples is not much. Within these samples, the optimized sample turn out to be 4% Yb^{3+} doped $Cs_2AgIn_{0.89}Bi_{0.11}Cl_6$ for getting highest intensity of NIR emission at 365 nm excitation.

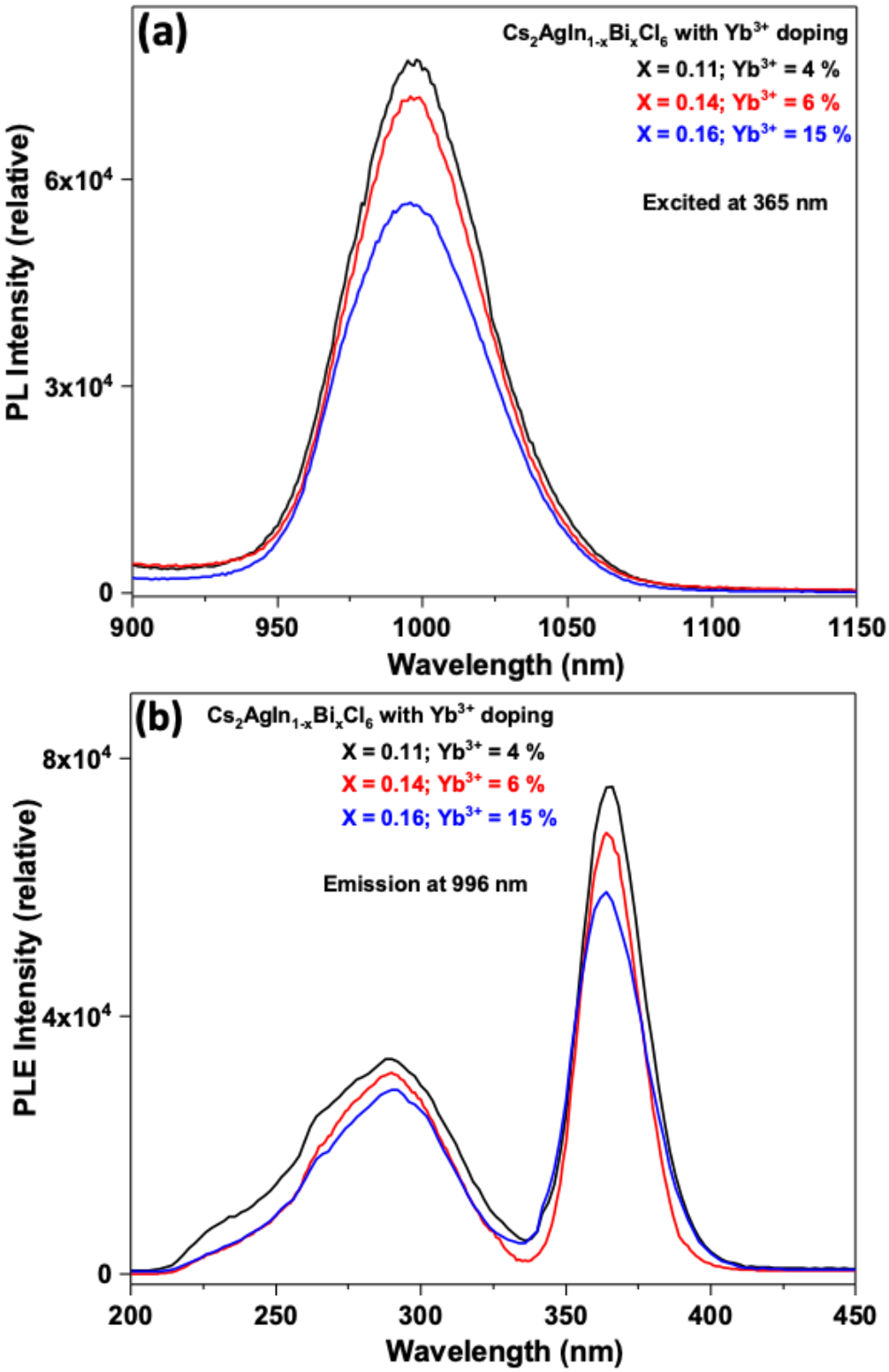

Fig. 14: NIR emission spectra (a) of Yb^{3+} doped $Cs_2AgIn_{1-x}Bi_xCl_6$ double perovskite NCs excited at 365 nm and PLE spectra (b) at ~996 nm emission.

Fig. 15 (a) shows the visible emission of Yb^{3+} doped $Cs_2AgIn_{1-x}Bi_xCl_6$ double perovskite NCs excited at 365 nm and PLE spectra (b) at ~630 nm emission. Here the visible

emission intensity increases slightly as the Yb^{3+} concentration increases from 4% (black) to 6% (red) and then decreased on further Yb^{3+} addition (Fig. 15 b). Therefore 6% Yb^{3+} doped $Cs_2AgIn_{0.86}Bi_{0.14}Cl_6$ (red) shows slightly higher emission in visible region then other two samples.

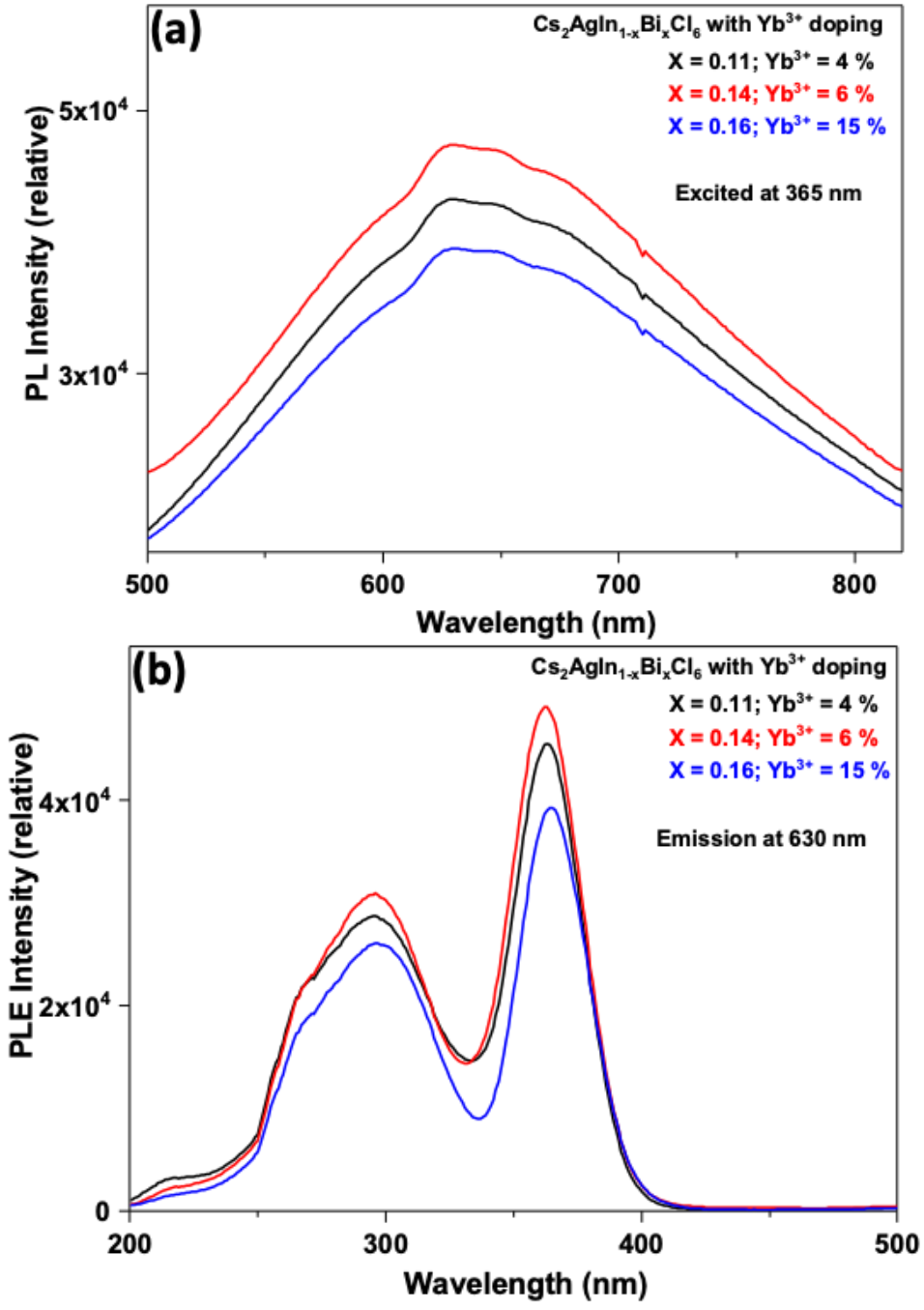

Fig. 15: Visible emission spectra (a) of Yb^{3+} doped $Cs_2AgIn_{1-x}Bi_xCl_6$ double perovskite NCs excited at 365 nm and PLE spectra (b) at ~630 nm emission.

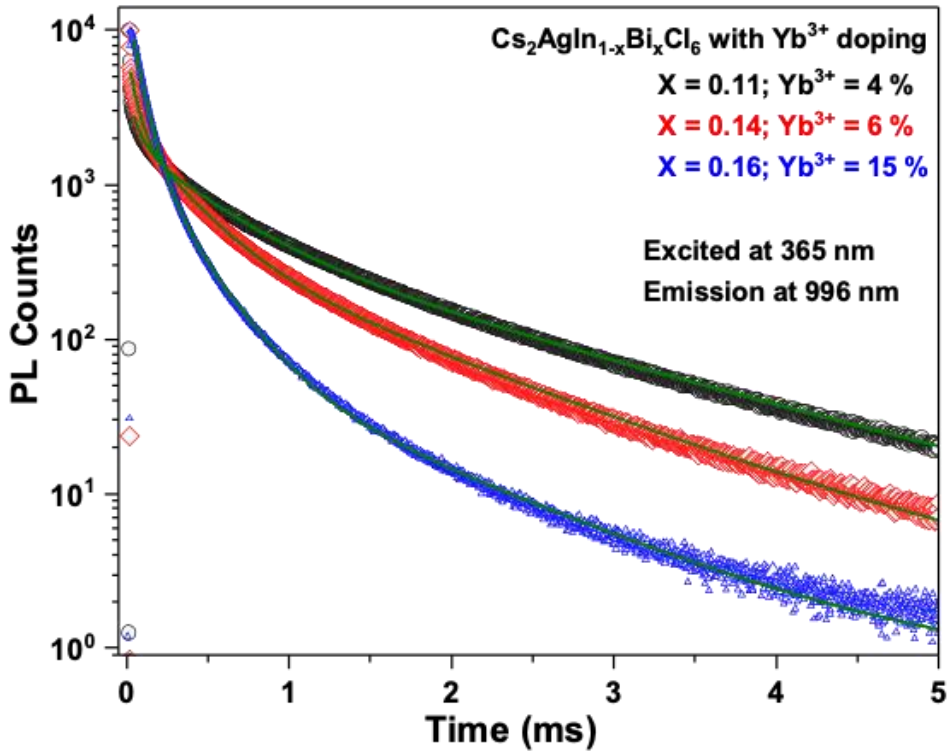

Fig. 16: PL decay dynamics of Yb^{3+} doped $Cs_2AgIn_{1-x}Bi_xCl_6$ double perovskite NCs excited at 365 nm and emission at 996 nm. A triexponential decay was used to fit the experimental PL decay data.

Table 3: Fitting parameters for PL decay lifetime of Yb^{3+} doped $Cs_2AgIn_{1-x}Bi_xCl_6$ double perovskite NCs excited at 365 nm.

	Yb^{3+} doped $Cs_2AgIn_{1-x}Bi_xCl_6$		
	x = 0.11	x = 0.14	x = 0.16
	Yb^{3+} = 4%	Yb^{3+} = 6%	Yb^{3+} = 15%
a_1	51%	66%	86%
τ_1 (µs)	61.4	50.9	70.7
a_2	36%	27%	13%
τ_2(µs)	417.8	290.7	242.5
a_3	13%	7%	1%
τ_3 (µs)	1484.4	1101.7	980.1
<τ> (µs)	**937.3**	**578.7**	**211**

PL decay plots of Yb^{3+} doped $Cs_2AgIn_{1-x}Bi_xCl_6$ double perovskite NCs are fitted with triexponential decay, as shown in Fig. 16. The best fits parameters are shown in Table

3. The long average lifetime in millisecond range is characteristics of Yb^{3+} Laporte forbidden $^2F_{5/2} \rightarrow {}^2F_{7/2}$ transition. Average lifetime (<τ>) is calculated by using the formula τ_{avg} (μs) = ($\Sigma a_i\tau_i^2/ \Sigma a_i\tau_i$). The average lifetime (<τ>) shows a decreasing trend with increasing concentration of Yb^{3+} doping. One plausible reason can be that, with the increasing Yb^{3+} concentration, the Yb^{3+}-Yb^{3+} interaction increases which can slightly decrease the radiative lifetime. But further understanding of these results are required.

4. Conclusions:

Colloidal NCs of Yb^{3+} doped $Cs_2AgIn_xBi_{1-x}Cl_6$ are prepared. XRD patterns confirm the phase purity of the samples. TEM images show cuboid nanocrystals of ~ 10 nm in size. Lattice fringes of HRTEM represent the crystallinity of the NCs. NIR emission at ~996 nm is obtained due to de-excitation of f electrons ($^2F_{5/2} \rightarrow {}^2F_{7/2}$) in Yb^{3+} dopant. Also, a broad emission in the visible region is obtained due to the STEs of the host. Optical absorbance and PLE data confirm the introduction of new excitation channel at lower energy (~365 nm = 3.4eV) on increasing the Bi^{3+} concentration in Yb^{3+} doped $Cs_2AgIn_xBi_{1-x}Cl_6$. PL in NIR and visible both has contribution of energy transfer from host $Cs_2AgIn_xBi_{1-x}Cl_6$ to the dopant and STE sites. Our optimized compositions for the most intense NIR emission with low excitation energy is 4% Yb^{3+} doped $Cs_2AgIn_{0.89}Bi_{0.11}Cl_6$. These NCs have potential for future applications in solution processed NIR LEDs and sensors.

References:

1. Kojima, A.; Teshima, K.; Shirai, Y.; Miyasaka, T., Organometal Halide Perovskites as Visible-Light Sensitizers for Photovoltaic Cells. J . Am. Chem. Soc. **2009,** *131*, 6050-6051.
2. Lee, M. M.; Teuscher, J.; Miyasaka, T.; Murakami, T. N.; Snaith, H. J., Efficient Hybrid Solar Cells Based on Meso-Superstructured Organometal Halide Perovskites. *Science* **2012,** *338*, 643-647.
3. Etgar, L.; Gao, P.; Xue, Z.; Peng, Q.; Chandiran, A. K.; Liu, B.; Nazeeruddin, M. K.; Grätzel, M., Mesoscopic CH3NH3PbI3/TiO2 Heterojunction Solar Cells. J . Am. Chem. Soc. **2012,** *134*, 17396-17399.

4. Protesescu, L.; Yakunin, S.; Bodnarchuk, M. I.; Krieg, F.; Caputo, R.; Hendon, C. H.; Yang, R. X.; Walsh, A.; Kovalenko, M. V., Nanocrystals of Cesium Lead Halide Perovskites (CsPbX3, X = Cl, Br, and I): Novel Optoelectronic Materials Showing Bright Emission with Wide Color Gamut. Nano Lett. **2015,** *15*, 3692-3696.

5. Swarnkar, A.; Chulliyil, R.; Ravi, V. K.; Irfanullah, M.; Chowdhury, A.; Nag, A., Colloidal CsPbBr3 Perovskite Nanocrystals: Luminescence beyond Traditional Quantum Dots. Angew. Chem., Int. Ed. **2015,** *54*, 15424-15428.

6. Manser, J. S.; Christians, J. A.; Kamat, P. V., Intriguing Optoelectronic Properties of Metal Halide Perovskites. Chem. Rev. **2016,** *116* (21), 12956-13008.

7. Sim, K. M.; Swarnkar, A.; Nag, A.; Chung, D. S., Phase Stabilized α-CsPbI3 Perovskite Nanocrystals for Photodiode Applications. Laser Photonics Rev. **2018,** *12*, 1700209.

8. Peng, L.; Dutta, S. K.; Mondal, D.; Hudait, B.; Shyamal, S.; Xie, R.; Mahadevan, P.; Pradhan, N., Arm Growth and Facet Modulation in Perovskite Nanocrystals. J . Am. Chem. Soc. **2019,** *141*, 16160-16168.

9. Krishnamoorthy, T.; Ding, H.; Yan, C.; Leong, W. L.; Baikie, T.; Zhang, Z.; Sherburne, M.; Li, S.; Asta, M.; Mathews, N.; Mhaisalkar, S. G., Lead-free germanium iodide perovskite materials for photovoltaic applications. J. Mater. Chem. A **2015,** *3*, 23829-23832.

10. Giustino, F.; Snaith, H. J., Toward Lead-Free Perovskite Solar Cells. ACS Energy Lett. **2016,** *1*, 1233-1240.

11. Chen, M.; Ju, M.-G.; Garces, H. F.; Carl, A. D.; Ono, L. K.; Hawash, Z.; Zhang, Y.; Shen, T.; Qi, Y.; Grimm, R. L.; Pacifici, D.; Zeng, X. C.; Zhou, Y.; Padture, N. P., Highly stable and efficient all-inorganic lead-free perovskite solar cells with native-oxide passivation. Nat. Commun. **2019,** *10*, 16.

12. Swarnkar, A.; Ravi, V. K.; Nag, A., Beyond Colloidal Cesium Lead Halide Perovskite Nanocrystals: Analogous Metal Halides and Doping. ACS Energy Lett. **2017,** *2*, 1089-1098.

13. Ravi, V. K.; Singhal, N.; Nag, A., Initiation and future prospects of colloidal metal halide double-perovskite nanocrystals: Cs2AgBiX6 (X = Cl, Br, I). J. Mater. Chem. A **2018,** *6*, 21666-21675.

14. Jellicoe, T. C.; Richter, J. M.; Glass, H. F. J.; Tabachnyk, M.; Brady, R.; Dutton, S. E.; Rao, A.; Friend, R. H.; Credgington, D.; Greenham, N. C.; Böhm, M.

L., Synthesis and Optical Properties of Lead-Free Cesium Tin Halide Perovskite Nanocrystals. J . Am. Chem. Soc. **2016,** *138*, 2941-2944.

15. Leng, M.; Chen, Z.; Yang, Y.; Li, Z.; Zeng, K.; Li, K.; Niu, G.; He, Y.; Zhou, Q.; Tang, J., Lead-Free, Blue Emitting Bismuth Halide Perovskite Quantum Dots. Angew. Chem., Int. Ed. **2016,** *55*, 15012-15016.

16. Xiao, Z.; Meng, W.; Wang, J.; Mitzi, D. B.; Yan, Y., Searching for promising new perovskite-based photovoltaic absorbers: the importance of electronic dimensionality. Mater. Horiz. **2017,** *4*, 206-216.

17. Pal, J.; Manna, S.; Mondal, A.; Das, S.; Adarsh, K. V.; Nag, A., Colloidal Synthesis and Photophysics of M3Sb2I9 (M=Cs and Rb) Nanocrystals: Lead-Free Perovskites. Angew. Chem., Int. Ed. **2017,** *56*, 14187-14191.

18. Pal, J.; Bhunia, A.; Chakraborty, S.; Manna, S.; Das, S.; Dewan, A.; Datta, S.; Nag, A., Synthesis and Optical Properties of Colloidal M3Bi2I9 (M = Cs, Rb) Perovskite Nanocrystals. J. Phys. Chem. C **2018,** *122*, 10643-10649.

19. Zhou, L.; Liao, J.-F.; Huang, Z.-G.; Wang, X.-D.; Xu, Y.-F.; Chen, H.-Y.; Kuang, D.-B.; Su, C.-Y., All-Inorganic Lead-Free Cs2PdX6 (X = Br, I) Perovskite Nanocrystals with Single Unit Cell Thickness and High Stability. ACS Energy Lett. **2018,** *3*, 2613-2619.

20. Tan, Z.; Li, J.; Zhang, C.; Li, Z.; Hu, Q.; Xiao, Z.; Kamiya, T.; Hosono, H.; Niu, G.; Lifshitz, E.; Cheng, Y.; Tang, J., Highly Efficient Blue-Emitting Bi-Doped Cs2SnCl6 Perovskite Variant: Photoluminescence Induced by Impurity Doping. Adv. Funct. Mater. **2018,** *28*, 1801131.

21. McClure, E. T.; Ball, M. R.; Windl, W.; Woodward, P. M., Cs2AgBiX6 (X = Br, Cl): New Visible Light Absorbing, Lead-Free Halide Perovskite Semiconductors. Chem. Mater. **2016,** *28*, 1348-1354.

22. Slavney, A. H.; Hu, T.; Lindenberg, A. M.; Karunadasa, H. I., A Bismuth-Halide Double Perovskite with Long Carrier Recombination Lifetime for Photovoltaic Applications. J . Am. Chem. Soc. **2016,** *138*, 2138-2141.

23. Zhao, X.-G.; Yang, J.-H.; Fu, Y.; Yang, D.; Xu, Q.; Yu, L.; Wei, S.-H.; Zhang, L., Design of Lead-Free Inorganic Halide Perovskites for Solar Cells via Cation-Transmutation. J . Am. Chem. Soc. **2017,** *139*, 2630-2638.

24. Volonakis, G.; Haghighirad, A. A.; Milot, R. L.; Sio, W. H.; Filip, M. R.; Wenger, B.; Johnston, M. B.; Herz, L. M.; Snaith, H. J.; Giustino, F., Cs2InAgCl6: A

New Lead-Free Halide Double Perovskite with Direct Band Gap. J. Phys. Chem. Lett. **2017,** *8*, 772-778.

25. K, N. N.; Nag, A., Synthesis and luminescence of Mn-doped Cs2AgInCl6 double perovskites. Chem. Commun. **2018,** *54*, 5205-5208.

26. Arfin, H.; Kaur, J.; Sheikh, T.; Chakraborty, S.; Nag, A., Bi3+-Ln3+ (Ln = Er and Yb) codoped Cs2AgInCl6 Double Perovskite Near Infrared Emitter. Angew. Chem., Int. Ed. **2020,** *n/a*.

27. Yang, B.; Mao, X.; Hong, F.; Meng, W.; Tang, Y.; Xia, X.; Yang, S.; Deng, W.; Han, K., Lead-Free Direct Band Gap Double-Perovskite Nanocrystals with Bright Dual-Color Emission. J . Am. Chem. Soc. **2018,** *140*, 17001-17006.

28. Luo, J.; Wang, X.; Li, S.; Liu, J.; Guo, Y.; Niu, G.; Yao, L.; Fu, Y.; Gao, L.; Dong, Q.; Zhao, C.; Leng, M.; Ma, F.; Liang, W.; Wang, L.; Jin, S.; Han, J.; Zhang, L.; Etheridge, J.; Wang, J.; Yan, Y.; Sargent, E. H.; Tang, J., Efficient and stable emission of warm-white light from lead-free halide double perovskites. Nature **2018,** *563*, 541-545.

29. Dave, K.; Fang, M. H.; Bao, Z.; Fu, H. T.; Liu, R. S., Recent Developments in Lead-Free Double Perovskites: Structure, Doping, and Applications. Chem. Asian. J. **2020,** *15*, 242-252.

30. Mahalingam, V.; Vetrone, F.; Naccache, R.; Speghini, A.; Capobianco, J. A., Colloidal Tm3+/Yb3+-Doped LiYF4 Nanocrystals: Multiple Luminescence Spanning the UV to NIR Regions via Low-Energy Excitation. Adv. Mater. **2009,** *21*, 4025-4028.

31. Artizzu, F., Near-Infrared Luminescent Lanthanide Complexes of Quinolinol Ligands: Structure/Properties Relationship. **2008**.

32. Mir, W. J.; Sheikh, T.; Arfin, H.; Xia, Z.; Nag, A., Lanthanide doping in metal halide perovskite nanocrystals: spectral shifting, quantum cutting and optoelectronic applications. *NPG Asia Materials* **2020,** *12*, 9.

33. Zhou, D.; Liu, D.; Pan, G.; Chen, X.; Li, D.; Xu, W.; Bai, X.; Song, H., Cerium and Ytterbium Codoped Halide Perovskite Quantum Dots: A Novel and Efficient Downconverter for Improving the Performance of Silicon Solar Cells. Adv. Mater. **2017,** *29*, 1704149.

34. Pan, G.; Bai, X.; Yang, D.; Chen, X.; Jing, P.; Qu, S.; Zhang, L.; Zhou, D.; Zhu, J.; Xu, W.; Dong, B.; Song, H., Doping Lanthanide into Perovskite Nanocrystals: Highly Improved and Expanded Optical Properties. Nano Lett. **2017,** *17*, 8005-8011.

35. Milstein, T. J.; Kroupa, D. M.; Gamelin, D. R., Picosecond Quantum Cutting Generates Photoluminescence Quantum Yields Over 100% in Ytterbium-Doped CsPbCl3 Nanocrystals. Nano Lett. **2018,** *18*, 3792-3799.
36. Mahor, Y.; Mir, W. J.; Nag, A., Synthesis and Near-Infrared Emission of Yb-Doped Cs2AgInCl6 Double Perovskite Microcrystals and Nanocrystals. J. Phys.Chem.C **2019,** *123*, 15787-15793.
37. Bekenstein, Y.; Dahl, J. C.; Huang, J.; Osowiecki, W. T.; Swabeck, J. K.; Chan, E. M.; Yang, P.; Alivisatos, A. P., The Making and Breaking of Lead-Free Double Perovskite Nanocrystals of Cesium Silver–Bismuth Halide Compositions. Nano Lett. **2018,** *18*, 3502-3508.
38. Liu, Y.; Jing, Y.; Zhao, J.; Liu, Q.; Xia, Z., Design Optimization of Lead-Free Perovskite Cs2AgInCl6:Bi Nanocrystals with 11.4% Photoluminescence Quantum Yield. Chem. Mater. **2019,** *31*, 3333-3339.
39. Li, T.; Zhao, X.; Yang, D.; Du, M.-H.; Zhang, L., Intrinsic Defect Properties in Halide Double Perovskites for Optoelectronic Applications. Phys. Rev.**2018,** *10*, 041001.

Copyright Permission

JOHN WILEY AND SONS LICENSE
TERMS AND CONDITIONS

Mar 14, 2020

This Agreement between NCL ("You") and John Wiley and Sons ("John Wiley and Sons") consists of your license details and the terms and conditions provided by John Wiley and Sons and Copyright Clearance Center.

License Number	4787530584865
License date	Mar 14, 2020
Licensed Content Publisher	John Wiley and Sons
Licensed Content Publication	Chemistry - An Asian Journal
Licensed Content Title	Recent Developments in Lead–Free Double Perovskites: Structure, Doping, and Applications
Licensed Content Author	Ru Shi Liu, Hong Ting Fu, Zhen Bao, et al
Licensed Content Date	Dec 16, 2019
Licensed Content Volume	15
Licensed Content Issue	2
Licensed Content Pages	11
Type of use	Dissertation/Thesis
Requestor type	University/Academic
Format	Print and electronic